MOCVD epitaxy of ultra-wide bandgap β-$(Al_xGa_{1-x})_2O_3$ with high-Al composition on (100) β-Ga_2O_3 substrates

A F M Anhar Uddin Bhuiyan[1], Zixuan Feng[1], Jared M. Johnson[2], Hsien-Lien Huang[2], Jinwoo Hwang[2], and Hongping Zhao[1,2,a)]

[1]*Department of Electrical and Computer Engineering, The Ohio State University, Columbus, OH 43210, USA*

[2]*Department of Materials Science and Engineering, The Ohio State University, Columbus, OH 43210, USA*

[a)]Corresponding author Email: zhao.2592@osu.edu

Single β-phase (100) $(Al_xGa_{1-x})_2O_3$ thin films were successfully grown on (100) oriented β-Ga_2O_3 substrates via metalorganic chemical vapor deposition (MOCVD). By systematically tuning the precursor molar flow rates and growth conditions including chamber pressure, growth temperature and group VI/III molar ratio, pure β-phase (100) $(Al_xGa_{1-x})_2O_3$ films with up to 52% of Al compositions were achieved. Comprehensive material characterization via X-ray diffraction (XRD) and high-resolution scanning transmission electron microscopy (HR-STEM) revealed high quality epitaxial growth of (100) β-$(Al_xGa_{1-x})_2O_3$ films on (100) native substrates. High resolution X-ray spectroscopy (XPS) was used for determining the AlGaO bandgaps and the Al compositions. Two-dimensional defects in the β-$(Al_xGa_{1-x})_2O_3$ films were investigated utilizing atomic resolution STEM imaging. Additionally, film characterization via HR-STEM imaging, XRD and energy-dispersive X-ray spectroscopy (STEM-EDS) revealed coherent growth of high quality (100) β-$(Al_xGa_{1-x})_2O_3/Ga_2O_3$ superlattice (SL) structures ($x \leq 50\%$) with abrupt interfaces and relatively uniform Al distribution. Step flow growth of (100) β-$(Al_xGa_{1-x})_2O_3$ with smooth and featureless surface morphology was observed in AlGaO samples with high-Al compositions. A mechanism for the step-flow growth of high-Al content β-$(Al_xGa_{1-x})_2O_3$ film is proposed by considering Al adatoms as preferred incorporation sites for AlGaO nucleation and growth.

Keywords: Ultra-wide bandgap, (100) β-$(Al_xGa_{1-x})_2O_3$ thin films, metalorganic chemical vapor deposition (MOCVD), $(Al_xGa_{1-x})_2O_3/Ga_2O_3$ superlattice

Introduction

β-Ga_2O_3 has an ultra-wide bandgap energy (~4.8 eV) with a theoretically predicted high breakdown field strength of 8 MV/cm [1]. Due to its higher thermal/chemical stability and n-type doping capability with excellent transport properties [2], β-Ga_2O_3 is predicted to outperform the current leading technology based on traditional wide bandgap semiconductors, such as SiC and GaN. Significant progress on the development of high quality β-Ga_2O_3 native substrates [3] and epitaxy [4-9] have been made since the first conceptual β-Ga_2O_3 device demonstration [10,11]. Owing to its outstanding material properties, high performance β-Ga_2O_3 based devices including lateral [12,13] and vertical field-effect transistors [14,15], Schottky barrier diodes [16-18] and ultraviolet solar blind photodetectors [19], have already been successfully demonstrated. Besides (010) β-Ga_2O_3 substrates, which has been widely explored for homoepitaxy of β-Ga_2O_3 thin films, larger size substrates become commercially available with other orientations such as (100), (001), and $(\bar{2}01)$ planes, motivating the understanding of materials epitaxy along different crystalline planes [3]. However, owing to the different surface energies of different surface planes of β-Ga_2O_3 [20], the understanding of homoepitaxial growth mechanism on different planes are still lacking.

While tremendous efforts on the growth of high quality β-Ga_2O_3 thin films have been made to demonstrate high performance electronic devices, there has been a limited work to date on the epitaxy of β-Ga_2O_3 based alloys and heterostructures. Recently, interest in Ga_2O_3-Al_2O_3 alloy in power and radio-frequency electronics has increased significantly due to its bandgap tunability up to 8.8 eV [21]. Because of its higher bandgap energy, β-$(Al_xGa_{1-x})_2O_3$ alloys can take advantage of a large critical electric field strength in not only vertical power devices but also in high-

performance lateral devices through device scaling. The promising transport properties of two-dimensional electron gases (2DEG) in heterostructures is of great interest in lateral devices. Recently, excellent mobility with high sheet charge density have been demonstrated in modulation doped field effect transistors (MODFETs) by forming 2DEG in AlGaO/GaO heterostructures where the Al composition in AlGaO layer was limited up to ~18% [22,23]. High quality AlGaO epitaxy with higher Al composition can maximize the electron mobility by separating the 2DEG from the ionized donor impurities [24]. While both the equilibrium phase diagram and theoretical studies have predicted that the solubility limit of Al_2O_3 in β-Ga_2O_3 as high as ~67% [25] and 71% [21], very limited Al incorporation in β-phase AlGaO alloys has been observed experimentally. Both MOCVD [26-29] and MBE [30] growth of (010) β-$(Al_xGa_{1-x})_2O_3$ film have indicated the maximum Al incorporation in β-phase is limited to < 27%. Targeting higher Al compositions in (010) β-$(Al_xGa_{1-x})_2O_3$ films has resulted in phase transformation [26], indicating the challenge for incorporating higher-Al in pure β-phase $(Al_xGa_{1-x})_2O_3$ film grown on (010) β-Ga_2O_3 substrate.

Although there are several reports on the epitaxial growth of high quality β-Ga_2O_3 films, the growth efforts on β-$(Al_xGa_{1-x})_2O_3$ film on different surface planes of β-Ga_2O_3 substrates are still limited. The coherent growth of β-$(Al_xGa_{1-x})_2O_3$ /β-Ga_2O_3 superlattice structures allow us to investigate the interface sharpness between the heterostructures and uniformity of the ternary β-$(Al_xGa_{1-x})_2O_3$ layers. Plasma-assisted MBE growth of γ-Al_2O_3/Ga_2O_3 superlattices on $MgAl_2O_4$ substrates [31] and α-Al_2O_3/Ga_2O_3 superlattices on r-plane sapphire substrates [32] revealed the possibility to obtain coherent heterostructures when optimize the sub-layer thickness and composition. Previous report on MOCVD growth of (010) β-$(Al_xGa_{1-x})_2O_3$ /β-Ga_2O_3 superlattice structures grown on (010) β-Ga_2O_3 substrates demonstrated Al composition of 21%, and characterized by XRD satellite peaks [33]. This study also claimed Al incorporation in (Al_xGa_{1-}

$_x)_2O_3$ films on sapphire substrates up to 43%, which was extracted from the absorption measurements, there were no XRD, TEM, or AFM data to determine the crystalline quality or phase of the $(Al_xGa_{1-x})_2O_3$ films. A recent pulsed-laser deposition (PLD) growth study has demonstrated (100) β-$(Al_xGa_{1-x})_2O_3$ epitaxy on (100) β-Ga_2O_3 substrates with up to 37% of Al compositions [34], and an MBE growth study revealed that (100) β-$(Al_xGa_{1-x})_2O_3$ films can maintain β-phase up to 61% of Al compositions [35], indicating the possibility of achieving higher Al composition in β-$(Al_xGa_{1-x})_2O_3$ alloy grown on (100) plane. However, the epitaxial growth of high-quality (100) β-$(Al_xGa_{1-x})_2O_3$ alloys and their atomic scale characterizations by utilizing high resolution STEM imaging are still missing. To the best of our knowledge, there are no prior reports of MOCVD epitaxy of (100) β-$(Al_xGa_{1-x})_2O_3$ films on (100) native substrates. In this study, we investigate the MOCVD growth of phase pure (100) β-$(Al_xGa_{1-x})_2O_3$ films and (100) β-$(Al_xGa_{1-x})_2O_3$/Ga_2O_3 superlattice structures on (100) β-Ga_2O_3 substrates with Al compositions up to 52%. The (100) plane of monoclinic β-Ga_2O_3 is a cleavage plane with a much larger *a* lattice constant of 1.22 nm, as compared to *b* and *c* of 0.30 nm and 0.58 nm, respectively [21]. Due to having the lowest surface free energy of the major crystal plans in β-Ga_2O_3 [20], the adatoms of precursor species are believed to have difficulties bonding to the (100) growth surface. The low incorporation efficiency of the adatoms on the (100) surface plane can lead to random nucleation and island formation during Ga_2O_3 growth. Previous MOCVD growth studies on in-plane (100) β-Ga_2O_3 substrates revealed challenges in growing high quality (100) β-Ga_2O_3 films [36]. The on-axis growth of a (100) β-Ga_2O_3 film was demonstrated with the formation of incoherent boundaries (twin lamellae) and stacking faults, which is due to the limited diffusion length of the surface adatoms and 2D island growth mode [36]. In this work, we propose to use Al adatom as the

preferred bonding species to the O atoms on the (100) growth surface, ultimately promoting the high-quality epitaxy of (100) β-$(Al_xGa_{1-x})_2O_3$ thin films on (100) β-Ga_2O_3 substrates.

Experimental Section

In this study, (100) β-$(Al_xGa_{1-x})_2O_3$ thin films on Fe doped semi-insulating (100) β-Ga_2O_3 substrates (from Novel Crystal Technology, Inc.) were grown via MOCVD and comprehensive material characterization was performed. Triethylgallium (TEGa), Trimethylaluminum (TMAl) and pure O_2 were used as Ga, Al and O precursors, respectively. Argon (Ar) was used as the carrier gas. The chamber pressure was varied between 20 torr and 80 torr. The growth temperature was tuned between 880 °C and 920 °C. Film thicknesses were varied between ~19 nm and ~85 nm. The growth rates of samples with different Al composition grown with different chamber pressures ranged between ~5.3 nm/min and ~13.3 nm/min. [TMAl]/[TEGa+TMAl] molar flow rate ratio was systematically tuned from 2.35% to 22.21%. The group VI/III ratio was varied between 908 and 1140. All substrates were treated with high temperature in-situ annealing for 10 minutes at 920°C under O_2 atmosphere prior epi-growth.

The crystal quality and the Al compositions of the films were evaluated with XRD measurements by a Bruker D8 Discover (Cu K_α radiation x-ray source, wavelength 1.5406A˚). Further Al composition measurement and the bandgap energies were derived from XPS utilizing a Kratos Axis Ultra X-ray photoelectron spectrometer with a monochromatized Al Kα x-ray source (E_{photon} = 1486.6 eV). The binding energy scale was referenced to C 1s core levels at 284.8 eV. High angle annular dark field (HAADF) STEM images of the samples were obtained by using a Thermo Fisher Scientific Titan scanning transmission electron microscopy operated at 300 kV. The microscope is also equipped with a quad-silicon drift detector (Super-X/ChemiSTEM) for X-

ray collection enabling EDS spectral mapping. The film thicknesses were estimated by both Pendellösung fringes observed from XRD spectra and high-resolution STEM images. Al compositions were confirmed by characterization through XRD, XPS and STEM-EDS mapping. The surface morphology and the surface roughness of the films were characterized via field emission scanning electron microscopy (FESEM, FEI Helios 600) and atomic force microscopy (AFM, Bruker AXS Dimension Icon), respectively.

Results and Discussion

Figure 1 shows the XRD spectra in ω-2θ scanning for (100) β-$(Al_xGa_{1-x})_2O_3$ films with different Al compositions. The films were grown by varying [TMAl]/[TEGa+TMAl] molar flow rate ratios from 2.35% to 22.21% and chamber pressures from 50 torr to 80 torr at 880 °C as listed in Table 1. The Al incorporations and the growth rates increase with increasing molar flow rate ratio. The sharp and high intensity X-ray diffraction peaks at $2\theta \approx 30.11°$ and 45.87°, as shown in Fig. 1, correspond to the signals originating from (400) and (600) reflections of (100) β-Ga_2O_3 substrates, respectively. The prominent characteristic diffraction peaks, marked by red and blue arrows, represent the (400) and (600) reflection peaks of (100) β-$(Al_xGa_{1-x})_2O_3$ films, respectively. With increasing Al compositions, the separations between the diffraction peak positions of the β-Ga_2O_3 substrate and the β-$(Al_xGa_{1-x})_2O_3$ films increase, indicating an increase in lattice mismatch between the substrate and the epi-films. The Al compositions were determined by analyzing the separations between the peak positions of the substrate and the epi-films, assuming fully coherent growth of (100) β-$(Al_xGa_{1-x})_2O_3$ films [21,37]. By the systematical tuning of [TMAl]/[TMAl+TEGa] molar flow ratios and chamber pressures, up to 52% Al incorporation in β-phase was identified from both (400) and (600) diffraction peaks of β-$(Al_xGa_{1-x})_2O_3$ films. At lower Al compositions, high intensity peaks with distinguishable Pendellösung fringes originated

from the epi-films indicate better crystalline quality of the films. With increasing Al compositions, the crystalline quality degrades, as evidenced by the decrease of the XRD peak intensities, broadening of the linewidths and lack of distinguishable Pendellösung fringes. However, the lower X-ray scattering factor of Al compared to Ga and relatively smaller thickness of high Al content samples can partially contribute to the weaker X-ray diffraction peak intensity at higher Al compositions [38]. Nevertheless, the degradation of crystalline quality of AlGaO film as Al composition increases is considered as the main mechanism of the reduction in XRD intensity.

In order to identify the elements in (100) β-$(Al_xGa_{1-x})_2O_3$ films and to estimate the Al compositions and bandgaps, high resolution XPS was performed on samples with different Al contents. Figure 2(a) shows the XPS survey spectra for a representative β-$(Al_{.47}Ga_{0.53})_2O_3$ film (Sample No. 4) in the binding energy range of 0 - 1200 eV. From the overall scan, no metallic contaminants in the films were detected, indicating high purity growth of the β-$(Al_{.47}Ga_{0.53})_2O_3$ film. The insets of Fig. 2(a) show the high resolution XPS spectra of Ga 3s and Al 2s core levels for samples with 15%, 33% and 47% Al content. With increasing of Al compositions, the peak intensity of Ga 3s core level reduces, while Al 2s core level increases; resulting in the increase of the Al/Ga intensity ratio. The Al compositions were determined by estimating the Ga and Al atomic concentrations from the Ga 3s and the Al 2s core level peak areas after applying atomic sensitivity factors [35]. The Al compositions calculated by XRD diffraction peak separations correlate well with the Al compositions estimated by XPS measurements as shown in Table 2. In the case of Sample No. 2 and 3, the Al compositions from XRD measurements (17% and 34%) which were calculated based on the assumption of fully strained films, indicate slight overestimates as compared to the Al compositions measured by XPS (15% and 33% Al). With ~80 nm (Sample No. 2) and ~44 nm (Sample No. 3) film thicknesses, the films may not be fully strained

(partial relaxation), which can result in the slight overestimation of the Al compositions [37]. By using XPS, the bandgap energies of (100) β-$(Al_xGa_{1-x})_2O_3$ films were also calculated. XPS can be used to analyze inelastic collisions that happen during photoexcitation and photoemission of electrons from the sample [39]. Due to these inelastic collisions such as band-to-band electronic transitions and excitation of "plasma waves" by columbic interaction with electrons in the valence band, the photo-excited electrons lose their final kinetic energy, which can be measured by XPS detector. These 'loss-spectra' peaks appeared as widened copies of the core-level peaks shifted towards higher binding energy relative to their original levels. As the fundamental lower limit of inelastic loss is equal to the bandgap energy, the onset of inelastic energy loss spectra relative to the core level peak corresponds to the bandgap energy [39-41]. By measuring the onset of inelastic loss relative to the O 1s core level peaks, the bandgaps of (100) β-$(Al_xGa_{1-x})_2O_3$ films with different Al compositions were estimated as shown in Figs. 2 (b)-(d). The energy corresponding to the onset of the loss spectra was estimated by calculating the intersection of the linear fitting of the loss spectra curve and its background 'zero' level which was determined by subtracting the Shirley background fitting [39]. The bandgap energies of β-$(Al_xGa_{1-x})_2O_3$ films with x = 15%, 33% and 47% were calculated as $E_g = 5.1 \pm 0.07$ eV, 5.4 ± 0.06 eV, and 5.7 ± 0.08 eV, respectively. The bandgap energies estimated by XPS measurement are found to be in close agreement with the values calculated by using first-principles hybrid density functional theory (DFT) [21,42], as listed in Table 2.

The surface morphology of β-$(Al_xGa_{1-x})_2O_3$ films were characterized by both FESEM and AFM imaging. Figures 3(a) and 3(b) show the surface view SEM images of two β-$(Al_xGa_{1-x})_2O_3$ films with 10% (Sample No. 1; ~53 nm thick) and 52% (Sample No. 6, ~20 nm thick) Al compositions, respectively. The films were grown by varying the TMAl molar flow rates with

optimized growth conditions. The SEM image for the sample with 10% Al composition shows the presence of granular protrusions on top surface as observed in Fig. 3(a), whereas the surface for the sample with higher Al composition (52%) exhibits less protrusions on top surface and relatively low root mean square (RMS) (Fig. 3(b)). While a recent PLD growth study of (100) β-$(Al_xGa_{1-x})_2O_3$ films indicates the formations of protrusions can be related to the quality of the target materials [34], we observed the surface of the epi-films becomes smoother with less protrusions when the Al incorporation increases. The surface morphology and RMS roughness for the samples with different Al compositions were also investigated by AFM imaging with scanning area of 5 μm x 5 μm. Figures 3(c)-(f) show the AFM images taken for β-$(Al_xGa_{1-x})_2O_3$ films with x = 10%, 34%, 47% and 52%, respectively. Previous reports on the MBE [35,43] and MOCVD [28] growths of β-$(Al_xGa_{1-x})_2O_3$ films on (010) [28,43] and (100) [35] β-Ga_2O_3 substrates have shown granular surface morphologies. As shown in Figs. 3(c)-(f), the AFM images exhibit similar granular morphologies, but with lower RMS roughness values ranging between 0.68 nm to 1.21 nm, indicating the growth of high quality (100) β-$(Al_xGa_{1-x})_2O_3$ films.

To further investigate the effect of higher Al incorporation in β-$(Al_xGa_{1-x})_2O_3$ films, the surface morphology of different samples grown with the same thickness (~170 nm) and same growth condition except with varied Al compositions are compared by FESEM images. Figures 4(a)-(d) show the surface view FESEM images of β-$(Al_xGa_{1-x})_2O_3$ films with Al composition of 10% to 49%. The films were grown at 880°C with the same chamber pressure (20 torr). At relatively lower Al compositions, the surface exhibits nonuniformity with bump like three-dimensional island structures. The Ga adatoms, due to the lack of energetically favorable nucleation sites, attach to other Ga adatoms and nucleate a new island, leading to the roughening of the surface, as observed in Figs. 4(a)-(b). As the Al molar flow rate increases, for example, in

the case of 49% Al, the surface uniformity is significantly enhanced, and the surface morphology evolves from three-dimensional surface roughness to progressive smoothness, as shown in Fig. 4(d). With relatively higher Al molar flow rates, Al adatoms provide more distribution of nucleation sites, which suppresses the 2D island growth mode and enhances the surface uniformity with smooth morphology. While obtaining smooth and flat surface is difficult on on-axis (100) β-Ga_2O_3 due to both surface anisotropy of the β-gallia structure [35] and lack of energetically favorable nucleation sites [36], we observed surface smoothing with increasing Al compositions, indicating a higher incorporation of Al adatoms on the growth surface can promote step-flow growth with surface homogeneity.

The schematic of the proposed step-flow growth mechanism, promoted by the incorporation of higher Al in (100) β-$(Al_xGa_{1-x})_2O_3$ film, is illustrated in Fig. 5. Previously, step-flow growth of β-Ga_2O_3 films was achieved on (100) native substrates only with higher miscut-angles, where the surface steps act as the preferred incorporation sites for the Ga adatoms [20,36]. While the lower adatom incorporation efficiency, due to the lack of energetically favorable lattice sites, such as surface steps or kinks, can lead to random nucleation and 2D island formation on on-axis (100) β-Ga_2O_3 substrates, as illustrated in Fig. 5(a), we propose a mechanism for step flow growth on on-axis (100) substrates, considering Al as a preferential nucleation bonding site for Ga adatoms and thus AlGaO growth. Figure 5(b) illustrates the processes involved in step-flow growth of β-$(Al_xGa_{1-x})_2O_3$ films on (100) native substrates. As Al adatoms have a much larger sticking coefficient than Ga adatoms [44], they are less likely to move on the growth surface from their point of impact from the vapor. As soon as the Al adatoms reach the growth surface, they are absorbed, nucleated, and distributed densely on the surface due to their higher affinity to oxidize as compared to Ga [45]. These densely distributed Al sites on the growth surface act as the

preferential nucleation sites for Ga adatoms and eventually promote the step-flow growth on in-plane (100) native substrates. Increasing the Al incorporation can provide more densely distributed Al sites, thus leading to the step flow growth of β-$(Al_xGa_{1-x})_2O_3$ film with enhanced surface smoothness and uniformity. Similarly, the uniform surface morphology due to higher Al incorporation can also be explained by the coalescence of the 2D islands. The densely distributed Al nucleation sites on the growth surface induce the Ga adatoms incorporation and more 2D islands formation. More Al nucleation sites can reduce the Ga adatoms diffusion to the top of the existing 2D islands, preventing the 3D growth mode. Thus, a uniform surface can be constructed through the coalescence of 2D islands as the growth proceeds.

Utilizing atomic resolution STEM, we analyze the exact structure, including extended defects, and composition of our β-$(Al_{0.17}Ga_{0.83})_2O_3$ film (Sample No. 2). Figure 6(a) shows a HAADF-STEM image of an 85 nm β-$(Al_{0.17}Ga_{0.83})_2O_3$ film grown on (100) β-Ga_2O_3. The lack of contrast within the film and at the interface suggests high-quality epitaxial growth of the film, correlating with the observed sharp peak in the XRD spectrum (Fig. 1). At higher magnification, as shown in Fig. 6(b), the HAADF image reveals the [010] cross-section of the β-phase film. Additionally, extended defects are observed at the atomic scale and are better shown in Figs. 6(c) and 6(d), which display the blue and orange regions, respectively, outlined in Fig. 6(b). The structure shown in Fig. 6(c) reveals a typical defect found in β-Ga_2O_3 bulk crystals and films – a twin [20, 46-48]. The twin boundary is marked with the red-dashed line, which lies in the (100) plane. This twin is detailed by a mirror at the boundary plane and a translation in the $[001]_m$. Previously, twin formation has been described by the double positioning mechanism [20]. This mechanism suggests a higher density of twins at smaller miscut-angles due to the predominant 2D island growth. Our films are grown with an ~ 0° miscut-angle, thus the formation of twins are

expected. Additionally, although the incorporation of Al promotes the step flow growth of the film, it may also play a key role in the development of defects like these twins. The defects shown in Fig. 6(d), extending in the $[001]_m$ for a half unit cell in growth direction, display twin boundaries in the (100) and (010) planes. At an (010) plane located within the thickness of the film foil, the crystal structure mirrors the matrix. This is depicted by overlaying the matrix structure (yellow outline) with the twinned structure (aqua outlined), resulting in staggered Ga atomic columns (green outline), which produces the intensities in our HAADF image. Immediately after the following half unit cell, the same defect is observed. An atomic column intensity analysis is still required to identify the role of Al on the formation of this defect. EDS performed on this film revealed a homogenous distribution of Al in the film with the expected ~15% incorporation (Fig. 6(e)).

We also characterize our β-$(Al_{0.52}Ga_{0.48})_2O_3$ film (Sample No. 6) grown on (100) β-Ga_2O_3 using STEM to determine the quality of its structure and composition. Figure 7 shows the results of HAADF-STEM imaging and EDS. The images in Figs. 7(a) and 7(b) show the epitaxial growth of the 20 nm (100) β-$(Al_{0.52}Ga_{0.48})_2O_3$ film. The contrast change in the film in both images results from the incorporation of the lighter Al species. However, as shown in Fig. 7(b), the Al tends to segregate rather than homogenously distribute amongst the film, which can be identified by the intensity variation. Additionally, a high density of twin boundaries and extended defects, such as those observed in the β-$(Al_{0.17}Ga_{0.83})_2O_3$ film, are scattered throughout the film. The local segregation of Al is also detected by EDS (Fig. 7(c)), with local composition ranging from 30% to 64%, with an average value of ~48%.

In addition to our efforts for the growth of (100) β-$(Al_xGa_{1-x})_2O_3$ thin films, we also investigated the growth of (100) β-$(Al_xGa_{1-x})_2O_3/Ga_2O_3$ superlattice (SL) structures with different

Al compositions. The SL structures grown with different [TMAl]/[TMAl + TEGa] molar flow rate ratios are summarized in Table 3. Figure 8(a) shows the schematic of the SL structure grown with 8 periods of AlGaO/GaO layers on top of an unintentionally doped (UID) 60 nm thick β-Ga_2O_3 buffer layer by targeting 50%, 40% and 17% of Al compositions in AlGaO barrier layers. The targeted thicknesses of AlGaO barrier layers for both 50% and 40% Al content SL structures were 5 nm with 10 nm of GaO well thicknesses (15 nm period), whereas for 17% Al content SL structure, the targeted barrier and well thicknesses were 15 nm and 10 nm, respectively (25 nm period). The structural quality and the abruptness of the AlGaO/GaO interfaces were evaluated from both (400) and (600) reflections of (100) β-$(Al_xGa_{1-x})_2O_3/Ga_2O_3$ SL structures by utilizing XRD spectra as shown in Figs. 8 (b)-(d). The high intensity satellites along with strong 0^{th} order peaks were observed from the XRD spectra. The SL structure grown with 17% Al composition shows up to 3^{rd} order of satellite peaks with strong 0^{th} order peak. With increasing Al contents, the 0^{th} order peak shifts towards higher 2θ angles, indicating the increase of average Al compositions for the entire SL structures. The average Al compositions calculated from the separation between the 0^{th} order peak and the substrate peak positions were 11.5%, 14.9% and 18.9% (corresponding targeted average Al compositions: 10.2%, 13.3%, and 16.7%) for x = 17%, 40% and 50%, respectively, and the periods estimated from the interval distances between adjacent satellite peaks were 26.6 nm, 14.6 nm, 14.1 nm (corresponding targeted periods: 25 nm, 15 nm, and 15 nm), respectively [49]. The average Al compositions and the periods calculated from XRD peak positions for each SL structures are found to be in a good agreement with the targeted average Al compositions of the entire superlattice structures and the periods. The XRD spectra for different Al compositions exhibit very sharp and distinguishable high order satellite peaks, indicating the

coherent growth of high quality superlattice structures with abrupt interfaces, even with 50% of Al compositions.

STEM imaging also revealed high-quality of the (100) β-$(Al_xGa_{1-x})_2O_3/Ga_2O_3$ superlattice structures. The AlGaO barrier layers in the SL structure were grown with targeted 50% Al compositions. HAADF-STEM images, shown in Figs. 9(a) and 9(b), display the alternating β-$(Al_xGa_{1-x})_2O_3/Ga_2O_3$ superlattice structure with sub-layers of ~5 nm β-$(Al_xGa_{1-x})_2O_3$ exhibiting dark contrast from the high Al concentration. The images show that the superlattice structure maintains the beta phase throughout the entire structure. The EDS color maps in Figs. 9(c) and 9(d) correspond to the Ga and Al concentrations from the plot in Fig. 9(e). This data demonstrates the alternating compositional profile of the periodic structure with the β-$(Al_xGa_{1-x})_2O_3$ layers. The Al content in β-$(Al_xGa_{1-x})_2O_3$ layer calculated by using the average Al composition (18.9%) and the period (14.1 nm) from the XRD measurement (Fig. 8) is found to be ~50%, the slight compositional deviation from EDS mapping can be related to the nonuniformity of Al distribution in $(Al_xGa_{1-x})_2O_3$ layers scanned along the direction indicated by the yellow arrow in 9(d).

Conclusion

In summary, we demonstrated MOCVD epitaxy of (100) β-$(Al_xGa_{1-x})_2O_3$ films and β-$(Al_xGa_{1-x})_2O_3/Ga_2O_3$ superlattice structures grown on (100) native substrates with up to 52% of Al compositions. High crystalline quality film with smooth surface morphology was achieved at high Al composition samples by systematical tuning of the growth parameters, including growth temperature, chamber pressure, VI/III ratio and etc. Cross sectional STEM images and EDS mapping for both thin films and superlattice structures exhibited abrupt GaO/AlGaO interfaces with homogenous Al distribution. Twin boundary defects were observed in the epitaxial films.

Smooth and uniform surface morphology observed for high Al composition samples revealed high quality step-flow growth promoted by higher Al incorporation where Al adatoms act as preferential nucleation sites for AlGaO growth. The successful development of high-quality epitaxy of pure β-$(Al_xGa_{1-x})_2O_3$ (100) films and β-$(Al_xGa_{1-x})_2O_3/Ga_2O_3$ superlattice structures with high-Al composition will enable device technologies based on this emerging ultrawide band gap semiconductor material system.

Acknowledgements

The authors acknowledge funding support from the Air Force Office of Scientific Research FA9550-18-1-0479 (AFOSR, Dr. Ali Sayir). Z. Feng and H. Zhao also acknowledge the National Science Foundation (Grant Nos. 1810041 and 2019753) for partial support. Electron microscopy was performed at the Center for Electron Microscopy and Analysis at The Ohio State University.

References

1. Higashiwaki, M.; Jessen, G. H. The dawn of gallium oxide microelectronics. *Appl. Phys. Lett.* **2018***, 112, 060401.*
2. Ma, N.; Tanen, N.; Verma, A.; Guo, Z.; Luo, T.; Xing, H.; Jena, D. Intrinsic electron mobility limits in β-Ga_2O_3. *Appl. Phys. Lett.* **2016***, 109(21), 212101*.
3. Kuramata, A.; Koshi, K.; Watanabe, S.; Yamaoka, Y.; Masui, T.; Yamakoshi, S. High-quality β-Ga_2O_3 single crystals grown by edge-defined film-fed growth. *Jpn. J. Appl. Phys.* **2016***, 55, 1202A2*.
4. Feng, Z.; Bhuiyan, A. F. M. A. U.; Karim, M. R.; Zhao, H. MOCVD homoepitaxy of Si-doped (010) β-Ga_2O_3 thin films with superior transport properties. *Appl. Phys. Lett.* **2019***, 114, 250601*.
5. Alema, F.; Zhang, Y.; Osinsky, A.; Valente, N.; Mauze, A.; Itoh, T.; Speck, J. S. Low temperature electron mobility exceeding 10^4 cm^2/V s in MOCVD grown β-Ga_2O_3. *APL Mater.* **2019***, 7, 121110*.

6. Baldini, M.; Albrecht, M.; Fiedler, A.; Irmscher, K.; Schewski, R.; Wagner, G. Si- and Sn-Doped Homoepitaxial β-Ga_2O_3 Layers Grown by MOVPE on (010)-Oriented Substrates. *ECS J. Solid State Sci. Technol.* **2017***, 6, Q3040*.
7. Rafique, S.; Han, L.; Tadjer, M. J.; Freitas, J. A., Jr.; Mahadik, N. A.; Zhao, H. Homoepitaxial growth of β-Ga_2O_3 thin films by low pressure chemical vapor deposition. *Appl. Phys. Lett.* **2016***, 108, 182105*.
8. Okumura, H.; Kita, M.; Sasaki, K.; Kuramata, A.; Higashiwaki, M.; Speck, J. S. Systematic investigation of the growth rate of β-Ga_2O_3(010) by plasma-assisted molecular beam epitaxy. *Appl. Phys. Express* **2014***, 7, 095501*.
9. Feng, Z.; Bhuiyan, A. F. M. A. U.; Xia, Z.; Moore, W.; Chen, Z.; McGlone, J. F.; Daughton, D. R.; Arehart, A. R.; Ringel, S. A.; Rajan, S.; Zhao, H. Probing Charge Transport and Background Doping in Metal-Organic Chemical Vapor Deposition-Grown (010) β-Ga_2O_3. Phys. Status Solidi RPL. **2020***, 14, 2000145*.
10. Higashiwaki, M.; Sasaki, K.; Kuramata, A.; Masui, T.; Yamakoshi, S. Gallium oxide (Ga_2O_3) metal-semiconductor field-effect transistors on single-crystal β-Ga_2O_3 (010) substrates. *Appl. Phys. Lett.* **2012***, 100, 013504*.
11. Higashiwaki, M.; Sasaki, K.; Kamimura, T.; Wong, M. H.; Krishnamurthy, D.; Kuramata, A.; Masui, T.; Yamakoshi, S. Depletion-mode Ga_2O_3 metal-oxide-semiconductor field-effect transistors on β-Ga_2O_3 (010) substrates and temperature dependence of their device characteristics. *Appl. Phys. Lett.* **2013***, 103, 123511*.
12. Xia, Z.; Xue, H.; Joishi, C.; McGlone, J.; Kalarickal, N. K.; Sohel, S. H.; Brenner, M.; Arehart, A.; Ringel, S.; Lodha, S.; Lu, W.; Rajan, S. β-Ga_2O_3 Delta-Doped Field-Effect Transistors With Current Gain Cutoff Frequency of 27 GHz. *IEEE Electron Device Lett.* **2019***, 40, 1052*.
13. Green, J.; Chabak, K. D.; Heller, E. R.; Fitch, R. C., Jr.; Baldini, M.; Fiedler, A.; Irmscher, K.; Wagner, G.; Galazka, Z. Tetlak, S. E.; Crespo, A.; Leedy, K.; Jessen, G. H. 3.8-MV/cm Breakdown Strength of MOVPE-Grown Sn-Doped β-Ga_2O_3 MOSFETs. *IEEE Electron Device Lett.* **2016***, 37, 902*.
14. Wong, M. H.; Goto, K.; Murakami, H.; Kumagai, Y.; Higashiwaki, M. Current Aperture Vertical beta -Ga_2O_3 MOSFETs Fabricated by N- and Si-Ion Implantation Doping. *IEEE Electron Device Lett.* **2019***, 40, 431-434*.
15. Hu, Z.; Nomoto, K.; Li, W.; Tanen, N.; Sasaki, K.; Kuramata, A.; Nakamura, T.; Jena, D.; Xing, H. G.; Enhancement-Mode Ga2O3 Vertical Transistors With Breakdown Voltage >1 kV. *IEEE Electron Device Lett.* **2018***, 39, 869-872*.
16. Konishi, K.; Goto, K.; Murakami, H.; Kumagai, Y.; Kuramata, A.; Yamakoshi, S.; Higashiwaki, M. 1-kV vertical Ga_2O_3 field-plated Schottky barrier diodes. *Appl. Phys. Lett.* **2017***, 110, 103506*.
17. Li, W.; Nomoto, K.; Hu, Z.; Jena, D.; Xing, H. G. Field-Plated Ga_2O_3 Trench Schottky Barrier Diodes With a $BV^2/ R_{on,sp}$ of up to 0.95 GW/cm^2. *IEEE Electron Device Lett.* **2020***, 41, 107-110.*

18. Joishi, C.; Rafique, S.; Xia, Z.; Han, L.; Krishnamoorthy, S.; Zhang, Y.; Lodha, S.; Zhao, H.; Rajan, S. Low-pressure CVD-grown β-Ga_2O_3 bevel-field-plated Schottky barrier diodes. Appl. *Phys. Express* **2018***, 11, 031101.*
19. Oshima, T.; Okuno, T.; Arai, N.; Suzuki, N.; Ohira, S.; Fujita, S. Vertical Solar-Blind Deep-Ultraviolet Schottky Photodetectors Based on β-Ga_2O_3 Substrates. *Appl. Phys. Express* **2008***, 1, 011202.*
20. Schewski, R.; Lion, K.; Fiedler, A.; Wouters, C.; Popp, A.; Levchenko, S. V.; Schulz, T.; Schmidbauer, M.; Anooz, S. B.; Gruneberg, R.; Galazka, Z.; Wagner, G.; Irmscher, K.; Scheffler, M.; Draxl, C.; Albrecht, M. Step-flow growth in homoepitaxy of β-Ga_2O_3 (100)-The influence of the miscut direction and faceting. *APL Mater.* **2019***, 7, 022515.*
21. Peelaers, H.; Varley, J. B.; Speck, J. S.; Van de Walle, C. G. Structural and electronic properties of Ga_2O_3-Al_2O_3 alloys. *Appl. Phys. Lett.* **2018***, 112, 242101*.
22. Krishnamoorthy, S.; Xia, Z.; Joishi, C.; Zhang, Y.; McGlone, J.; Johnson, J.; Brenner, M.; Arehart, A. R.; Hwang, J.; Lodha, S.; Rajan, S. Modulation-doped β-$(Al_{0.2}Ga_{0.8})_2O_3$/Ga_2O_3 field-effect transistor. Appl. Phys. Lett. **2017**, 111, 023502.
23. Zhang, Y.; Neal, A.; Xia, Z.; Joishi, C.; Johnson, J. M.; Zheng, Y.; Bajaj, S.; Brenner, M.; Dorsey, D.; Chabak, K.; Jessen, G.; Hwang, J.; Mou, S.; Heremans, J. P.; Rajan, S. Demonstration of high mobility and quantum transport in modulation-doped β-$(Al_xGa_{1-x})_2O_3$/Ga_2O_3 heterostructures. *Appl. Phys. Lett.* **2018***, 112, 173502.*
24. Ghosh K.; Singisetti, U. Electron mobility in monoclinic β-Ga_2O_3 - Effect of plasmon-phonon coupling, anisotropy, and confinement. *J. Mater. Res.* **2017***, 32, 4142.*
25. Hill, V. G.; Roy, R.; Osborn, E. F. The System Alumina-Gallia-Water. *J. Am. Ceram. Soc.* **1952***, 35, 135.*
26. Bhuiyan, A. F. M. A. U.; Feng, Z.; Johnson, J. M.; Huang, H.-L.; Sarker, J.; Zhu, M.; Karim, M. R.; Mazumder, B.; Hwang, J.; Zhao, H. Phase transformation in MOCVD growth of $(Al_xGa_{1-x})_2O_3$ thin films. *APL Mater.* **2020***, 8, 031104*.
27. Ranga, P.; Rishinaramangalam, A.; Varley, J.; Bhattacharyya, A.; Feezell, D.; Krishnamoorthy, S. Si-doped β-$(Al_{0.26}Ga_{0.74})_2O_3$ thin films and heterostructures grown by metalorganic vapor-phase epitaxy. *Appl. Phys. Express* **2019***, 12, 111004*.
28. Bhuiyan, A. F. M. A. U.; Feng, Z.; Johnson, J. M.; Chen, Z.; Huang, H.-L.; Hwang, J.; Zhao, H. MOCVD epitaxy of β-$(Al_xGa_{1-x})_2O_3$ thin films on (010) Ga_2O_3 substrates and N-type doping. *Appl. Phys. Lett.* **2019***, 115, 120602.*
29. Sarkar, J.; Broderick, S.; Bhuiyan, A. F. M. A. U.; Feng, Z.; Zhao, H.; Mazumder, B. A combined approach of atom probe tomography and unsupervised machine learning to understand phase transformation in $(Al_xGa_{1-x})_2O_3$. *Appl. Phys. Lett.* **2020***, 116, 152101.*
30. Vogt, P.; Mauze, A.; Wu, F.; Bonef, B.; Speck, J. S. Metal-oxide catalyzed epitaxy (MOCATAXY): the example of the O plasma-assisted molecular beam epitaxy of β-$(Al_xGa_{1-x})_2O_3$/β-Ga_2O_3 heterostructures. *Appl. Phys. Express* **2018***, 11, 115503*.
31. Kato, Y.; Imura, M.; Nakayama, Y., Takeguchi, M.; Oshima, T. Fabrication of coherent γ-Al_2O_3/Ga_2O_3 superlattices on $MgAl_2O_4$ substrates. *Appl. Phys. Express* **2019***, 12, 065503*.

32. Oshima, T.; Kato, Y.; Imura, M.; Nakayama, Y.; Takeguchi, M. α-Al_2O_3/Ga_2O_3 superlattices coherently grown on r-plane sapphire. *Appl. Phys. Express* **2018***, 11, 065501.*
33. Miller, R.; Alema, F.; Osinsky, A.; Epitaxial β-Ga_2O_3 and β-$(Al_xGa_{1-x})_2O_3/$β-Ga_2O_3 Heterostructures Growth for Power Electronics. *IEEE Trans. Semicond. Manuf*. **2018***, 31(4), 467.*
34. Wakabayashi, R.; Hattori, M.; Yoshimatsu, K.; Horiba, K.; Kumigashira, H.; Ohtomo, A. Band alignment at β-$(Al_xGa_{1-x})_2O_3/$β-Ga_2O_3 (100) interface fabricated by pulsed-laser deposition. *Appl. Phys. Lett.* **2018***, 112, 232103.*
35. Oshima, T.; Okuno, T.; Arai, N.; Kobayashi, Y.; Fujita, S. β-$Al_{2x}Ga_{2-2x}O_3$ Thin Film Growth by Molecular Beam Epitaxy. *Jpn. J. Appl. Phys.* **2009***, 48, 070202*.
36. Schewski, R.; Baldini, M.; Irmscher, K.; Fiedler, A.; Markurt, T.; Neuschulz, B.; Remmele, T.; Schulz, T.; Wagner, G.; Galazka, Z.; Albrecht, M. Evolution of planar defects during homoepitaxial growth of β-Ga_2O_3 layers on (100) substrates - A quantitative model. *J. Appl. Phys.* **2016***, 120, 225308.*
37. Oshima, Y.; Ahmadi, E.; Badescu, S. C.; Wu, F.; Speck, J. S. Composition determination of example of the O plasma-assisted molecular beam epitaxy of β-$(Al_xGa_{1-x})_2O_3$ layers coherently grown on (010) β-Ga_2O_3 substrates by high-resolution X-ray diffraction. *Appl. Phys. Express* **2016***, 9, 061102*.
38. Kaneko, K.; Suzuki, K.; Ito, Y.; Fujita, S. Growth characteristics of corundum-structured α-$(Al_xGa_{1-x})_2O_3/$β-Ga_2O_3 heterostructures on sapphire substrates. *J. Cryst. Growth* **2016***, 436, 150*.
39. Nichols, M. T.; Li, W.; Pei, D.; Antonelli, G. A.; Lin, Q.; Banna, S.; Nishi, Y.; Shohet, J. L. Measurement of bandgap energies in low-k organosilicates. *J. Appl. Phys.* **2014***, 115, 094105*.
40. Zhang, F.; Saito, K.; Tanaka, T.; Nishio, M.; Arita, M.; Guo, Q. Wide bandgap engineering of $(AlGa)_2O_3$ films. *Appl. Phys. Lett. 105,* **2014***, 162107*.
41. Fares, C.; Ren, F.; Lambers, E.; Hays, D. C.; Gila, B. P.; Pearton, S. J. Band alignment of atomic layer deposited SiO_2 on (010) $(Al_{0.14}Ga_{0.86})_2O_3$. *J. Vac. Sci. Technol.* **2018***, 36, 061207*.
42. Peelaers, H.; Varley, J. B.; Speck, J. S.; Van de Walle, C. G. Erratum: "Structural and electronic properties of Ga2O3-Al2O3 alloys" [Appl. Phys. Lett. 112, 242101 (2018)]. *Appl. Phys. Lett.* **2019***, 115, 159901.*
43. Kaun, S. W.; Wu, F.; Speck, J. S. β-$(Al_xGa_{1-x})_2O_3/$β-Ga_2O_3 (010) heterostructures grown on β-Ga_2O_3 (010) substrates by plasma-assisted molecular beam epitaxy. *J. Vac. Sci. Technol.* **2015***, 33, 041508.*
44. Khan, M. A.; Shatalov, M.; Maruska, H. P.; Wang, H. M.; Kuokstis, E. III-Nitride UV Devices. *Jpn. J. Appl. Phys.* **2005***, 44, 7191.*
45. Luo, Y. R. Bond Dissociation Energies in CRC Handbook of Chemistry and Physics, 90th ed., edited by D. R. Lide (CRC Press/Taylor and Francis, Boca Raton, 2009).

46. Fiedlera, A.; Schewski, R.; Baldini, M.; Galazka, Z.; Wagner, G.; Albrecht, M.; Irmscher, K. Influence of incoherent twin boundaries on the electrical properties of β-Ga_2O_3 layers homoepitaxially grown by metal-organic vapor phase epitaxy. *J. Appl. Phys.* **2017***, 122, 165701.*
47. Gao, S.; Wu, Y.; Kanga, R.; Huang, H. Nanogrinding induced surface and deformation mechanism of single crystal β-Ga_2O_3. *Mater Sci Semicond Process* **2018***, 79, 165*.
48. Ueda, O.; Ikenaga, N.; Koshi, K.; Iizuka, K.; Kuramata, A.; Hanada, K.; Moribayashi, T.; Yamakoshi, S.; Kasu, M. Structural evaluation of defects in β-Ga_2O_3 single crystals grown by edge-defined film-fed growth process. *Jpn. J. Appl. Phys.* **2016***, 55 1202BD.*
49. Wen, T.-C.; Lee, W.-I. Influence of Barrier Growth Temperature on the Properties of InGaN/GaN Quantum Well. *Jpn. J. Appl. Phys.* **2001***, Part 1 40, 5302.*

Table Captions

Table 1. Summary of (100) β-$(Al_xGa_{1-x})_2O_3$ samples (shown in Fig. 1) grown with different [TMAl]/[TMAl + TEGa] molar flow rate ratios and chamber pressures with corresponding Al compositions, film thicknesses and growth rates.

Table 2. Summary of the Al contents and the bandgaps of (100) β-$(Al_xGa_{1-x})_2O_3$ samples, estimated from XRD and XPS characterization. The calculated direct and indirect bandgaps of β-$(Al_xGa_{1-x})_2O_3$ samples with different Al content are also listed from ref. [21,42]. The errors in the bandgaps measured from XPS are defined as the root-mean-square errors.

Table 3 Summary of (100) β-$(Al_xGa_{1-x})_2O_3$/β-Ga_2O_3 superlattice structures (shown in Fig. 8) grown with different [TMAl]/[TMAl + TEGa] molar flow rate ratio and the corresponding Al composition, barrier and well thickness.

Figure Captions

Figure 1 XRD ω-2θ patterns for the (400) and (600) reflections of β-$(Al_xGa_{1-x})_2O_3$ films grown on (100) β-Ga_2O_3 substrates. Sharp peaks at 30.11° and 45.86° indicate the (400) and (600) reflections from β-Ga_2O_3 substrates. Red and blue arrows indicate the XRD peak positions for the (400) and (600) reflections of β-$(Al_xGa_{1-x})_2O_3$ films with x ranging from 10% to 52%.

Figure 2 (a) XPS wide scan spectra of (100) β-$(Al_{0.47}Ga_{0.53})_2O_3$ showing the element specific peaks. The insets show the photoemission peaks of Ga 3s and Al 2s core levels for Al composition of x = 47% (blue), 33% (red) and 15% (black). The corresponding bandgap of (100) β-$(Al_xGa_{1-x})_2O_3$ films determined by the energy difference between O 1s core level peak and the onset of energy loss spectrum for (b) x = 15%, (c) x = 33%, and (d) x = 47%.

Figure 3 Surface view FESEM images of (100) β-$(Al_xGa_{1-x})_2O_3$ films grown on (100) β-Ga_2O_3 substrates with Al compositions of (a) x = 10%, and (b) x = 52% with film thicknesses of 53 nm and 20 nm, respectively. The surface topographic images of (100) β-$(Al_xGa_{1-x})_2O_3$ films with (c) x = 10%, (d) x = 34%, (e) x = 47%, and (f) x = 52% measured by AFM. The scan area is 5 x 5 μm^2.

Figure 4 Surface view FESEM images of ~170 nm thick (100) β-$(Al_xGa_{1-x})_2O_3$ films grown with Al compositions of (a) x = 10%, (b) x = 17%, (c) x = 44% and (d) x = 49%. The films were grown epitaxially on (100) β-Ga_2O_3 substrates at 880°C with chamber pressure of 20 Torr.

Figure 5 Schematic illustrations of the proposed growth mechanism of (100) β-$(Al_xGa_{1-x})_2O_3$ films grown on (100) β-Ga_2O_3 substrates: (a) typical 2D island mode growth processes of (100) β-Ga_2O_3 films on (100) on-axis β-Ga_2O_3 substrates including (1) the absorption and diffusion of Ga adatoms and (2) formation of 3D islands by the encounter of Ga adatoms due to the lack of energetically favorable lattice sites, such as surface steps or kinks and (b) step flow growth processes of high Al content (100) β-$(Al_xGa_{1-x})_2O_3$ films on (100) on-axis β-Ga_2O_3 substrates

include (1) absorption, diffusion and fast adherence of Al adatoms on the growth surface and (2) incorporation of Ga adatoms at the nearest Al site, which acts as the preferential nucleation site for incoming Ga adatoms.

Figure 6 High resolution HAADF-STEM images and EDS taken from the $[010]_m$ zone axis of an 85 nm thick β-$(Al_{0.17}Ga_{0.83})_2O_3$ film with a 60 nm thick (100) β-Ga_2O_3 buffer layer grown on top of a (100) β-Ga_2O_3 substrate. (a) Low magnification image with 50 nm scale displaying each interface. (b) Atomic resolution image of the β-$(Al_{0.17}Ga_{0.83})_2O_3$ film with (c) blue and (d) orange marked defect regions. (c) HAADF-STEM image of a (100) twin boundary (red-dashed line) and structure accompanied with a model. (d) Half unit cell thick defects extended in the $[001]_m$. Yellow-outlined and aqua-outlined models overlapped (green-outlined) represent the defect formation. (e) STEM-EDS profiles for Al (blue), Ga (green) and O (red) in the (100) β-$(Al_{0.17}Ga_{0.83})_2O_3$ film from the yellow region in (a).

Figure 7 High resolution HAADF-STEM images taken from the $[010]_m$ zone axis of the 20 nm thick β-$(Al_{0.52}Ga_{0.48})_2O_3$ film with 60 nm thick (100) β-Ga_2O_3 buffer layer grown on top of (100) β-Ga_2O_3 substrate at (a) 20 nm and (b) 5 nm scales. (c) STEM-EDS profiles for Al (blue), Ga (green) and O (red) in the (100) β-$(Al_{0.52}Ga_{0.48})_2O_3$ film from the yellow region in (a).

Figure 8 (a) Schematic of the 8 period (100) β-$(Al_xGa_{1-x})_2O_3$/β-Ga_2O_3 superlattice structures grown with 60 nm thick (100) β-Ga_2O_3 buffer layer on (100) β-Ga_2O_3 substrate. XRD ω-2θ scan profiles for (400) and (600) reflections (100) β-$(Al_xGa_{1-x})_2O_3$/β-Ga_2O_3 superlattice structures with Al composition of (b) 50% (blue), (c) 40% (red) and (d) 17% (black).

Figure 9 High resolution HAADF-STEM images of the 8-period β-$(Al_{0.50}Ga_{0.50})_2O_3$/β-$Ga_2O_3$ superlattice grown on (100) β-Ga_2O_3 substrate at (a) 20 nm, (b) 5 nm scales and associated EDS maps for (c) Ga and (d) Al. (e) The STEM-EDS line profiles for Al (blue), Ga (green) and O (red) along the direction indicated by the yellow arrow in (d).

Table 1

Sample No.	[TMAl]/[TMAl +TEGa] (%)	Al composition (%)	Chamber pressure (Torr)	Film Thickness (nm)	Growth rate (nm/min)
1	2.35	10	80	~53	5.3
2	3.82	17	80	~85	8.5
3	10.36	34	60	~44	8.8
4	18.08	47	50	~38	9.5
5	20.20	50	50	~19	9.5
6	22.21	52	50	~20	13.3

Table 2

Sample No.	**Al content (XRD) (%)**	**Al content (XPS) (%)**	**Bandgap (XPS) (eV)**	**Bandgap** [21,42] **(eV)**
2	17	15	5.1 ± 0.07	5.09^{direct}, $5.10^{indirect}$
3	34	33	5.4 ± 0.06	5.44^{direct}, $5.44^{indirect}$
4	47	47	5.7 ± 0.08	5.77^{direct}, $5.75^{indirect}$

Table 3

Superlattice structure No.	[TMAl]/[TMAl +TEGa] (%)	Number of periods	β-$(Al_xGa_{1-x})_2O_3$ barrier thickness (nm)	β-Ga_2O_3 well thickness (nm)	Targeted Al composition in barrier layer (%)
1	3.82	8	15	10	17
2	14.22	8	5	10	40
3	20.20	8	5	10	50

Figure 1

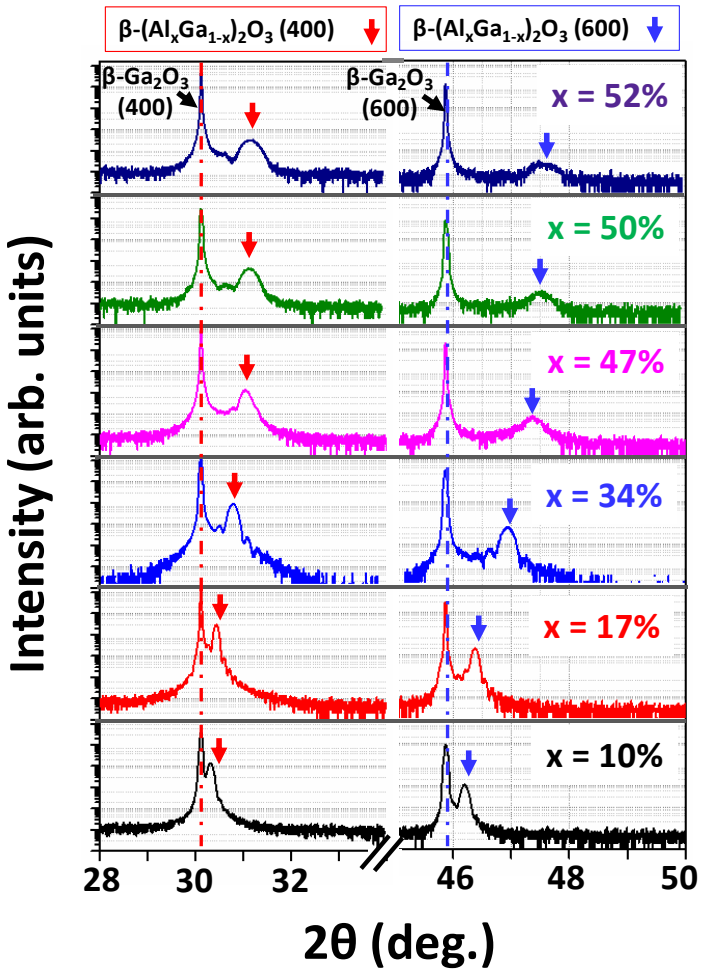
β-(AlxGa1-x)2O3 (400)
β-(AlxGa1-x)2O3 (600)
β-Ga2O3 (400)
β-Ga2O3 (600)
x = 52%
x = 50%
x = 47%
x = 34%
x = 17%
x = 10%
Intensity (arb. units)
28
30
32
46
48
50
2θ (deg.)

Figure 2

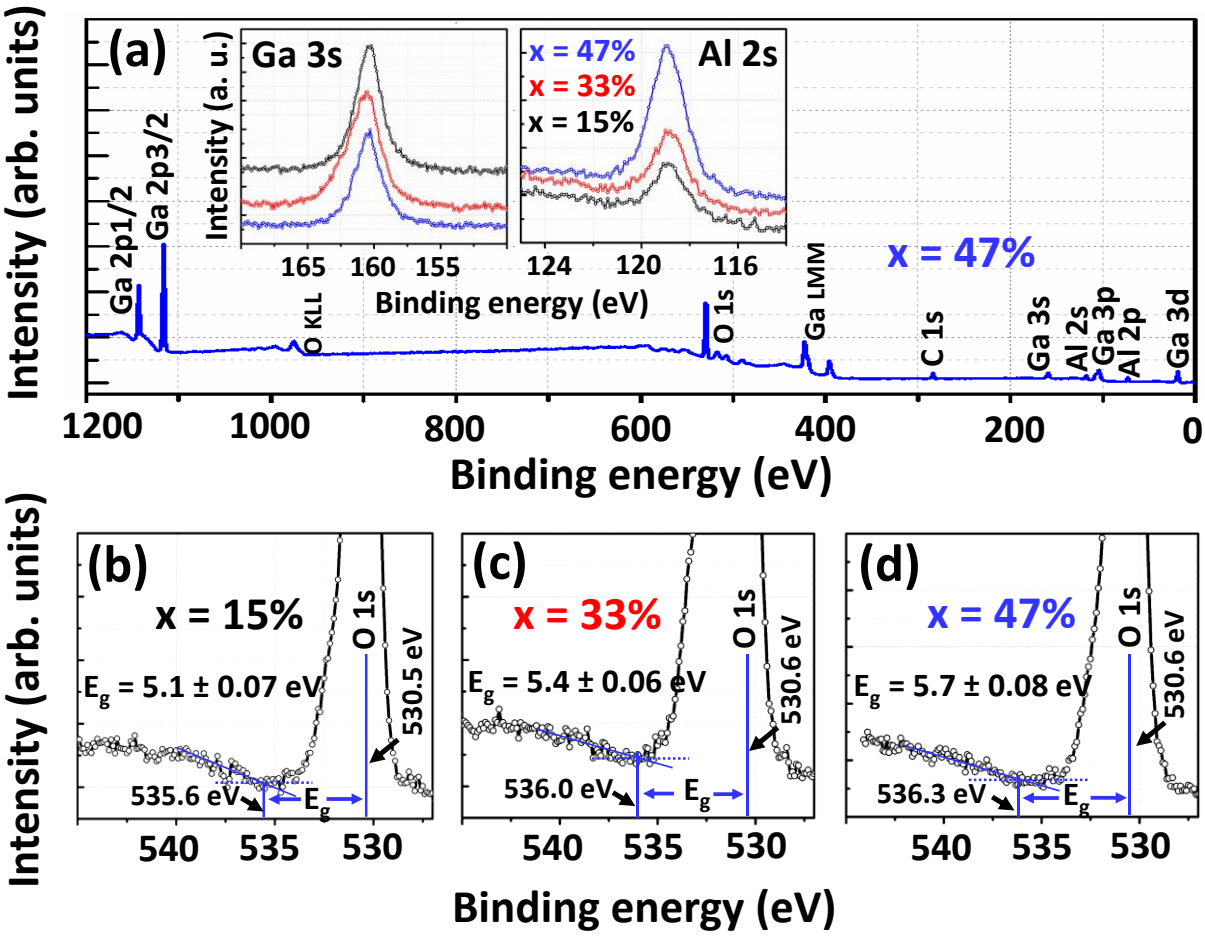
(a)
Ga 3s
Intensity (a. u.)
x = 47%
x = 33%
x = 15%
Al 2s
165 160 155
124 120 116
Binding energy (eV)
Intensity (arb. units)
Ga 2p1/2
Ga 2p3/2
O KLL
O 1s
Ga LMM
C 1s
Ga 3s
Al 2s
Ga 3p
Al 2p
Ga 3d
x = 47%
1200 1000 800 600 400 200 0
Binding energy (eV)
(b)
x = 15%
Eg = 5.1 ± 0.07 eV
O 1s
530.5 eV
535.6 eV
Eg
(c)
x = 33%
Eg = 5.4 ± 0.06 eV
O 1s
530.6 eV
536.0 eV
Eg
(d)
x = 47%
Eg = 5.7 ± 0.08 eV
O 1s
530.6 eV
536.3 eV
Eg
Intensity (arb. units)
540 535 530
Binding energy (eV)

Figure 3

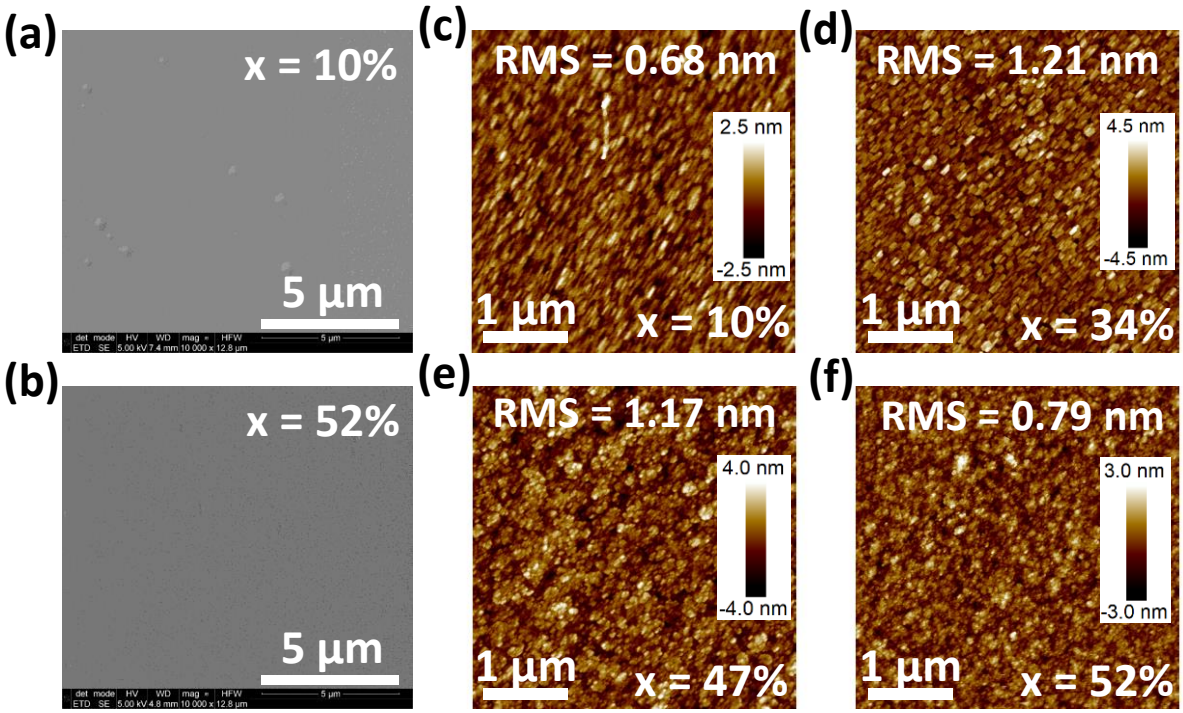
(a)
x = 10%
5 µm
(b)
x = 52%
5 µm
(c)
RMS = 0.68 nm
2.5 nm
-2.5 nm
1 µm
x = 10%
(d)
RMS = 1.21 nm
4.5 nm
-4.5 nm
1 µm
x = 34%
(e)
RMS = 1.17 nm
4.0 nm
-4.0 nm
1 µm
x = 47%
(f)
RMS = 0.79 nm
3.0 nm
-3.0 nm
1 µm
x = 52%

Figure 4

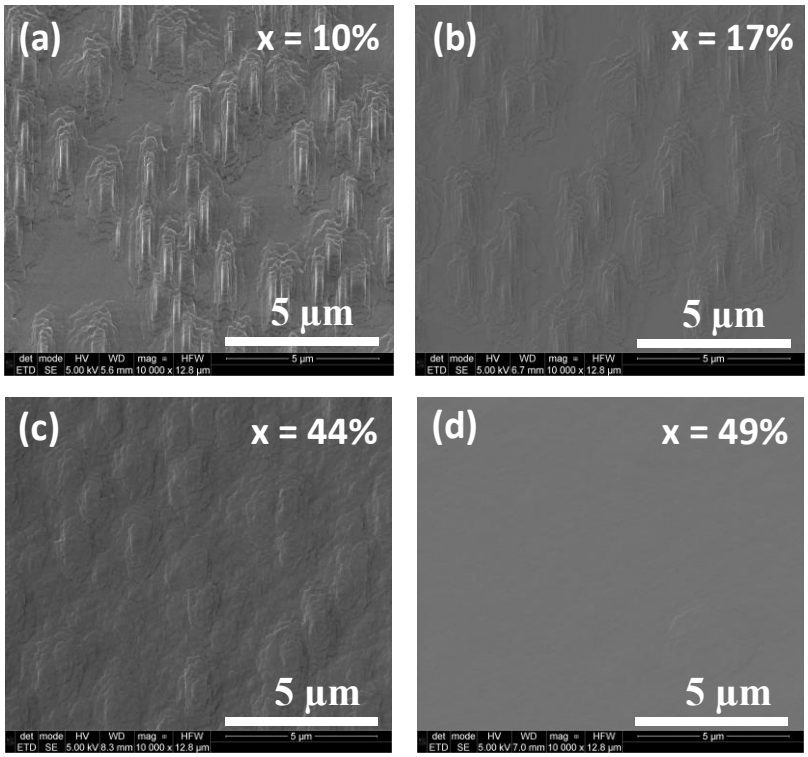

Figure 5

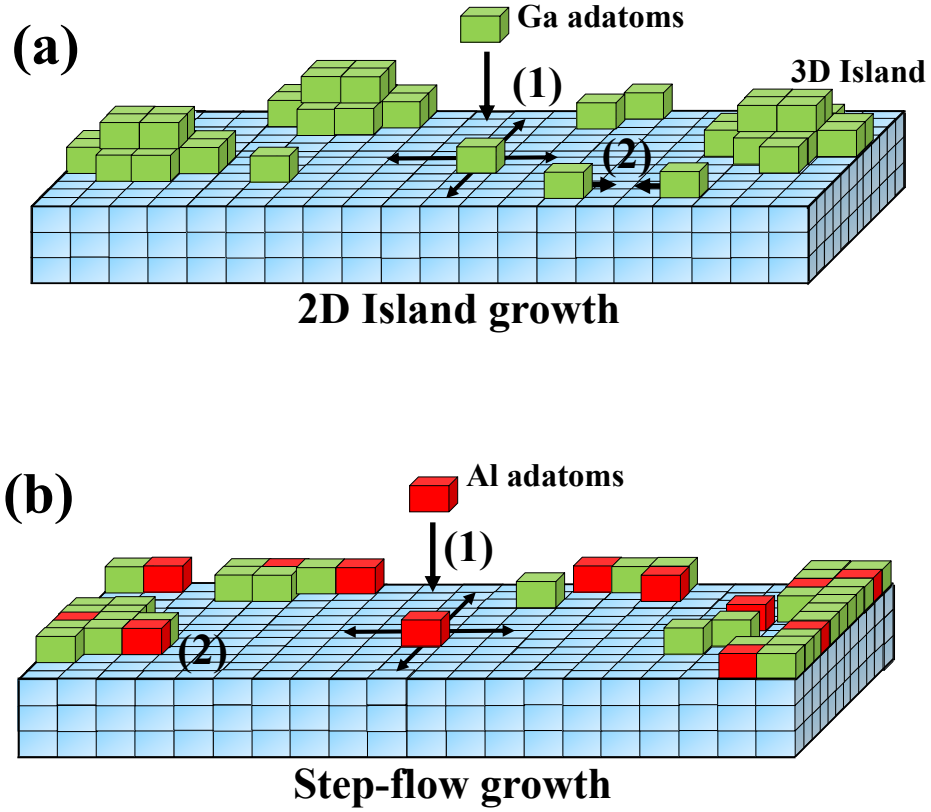
(a)
Ga adatoms
(1)
3D Island
(2)
2D Island growth
(b)
Al adatoms
(1)
(2)
Step-flow growth

Figure 6

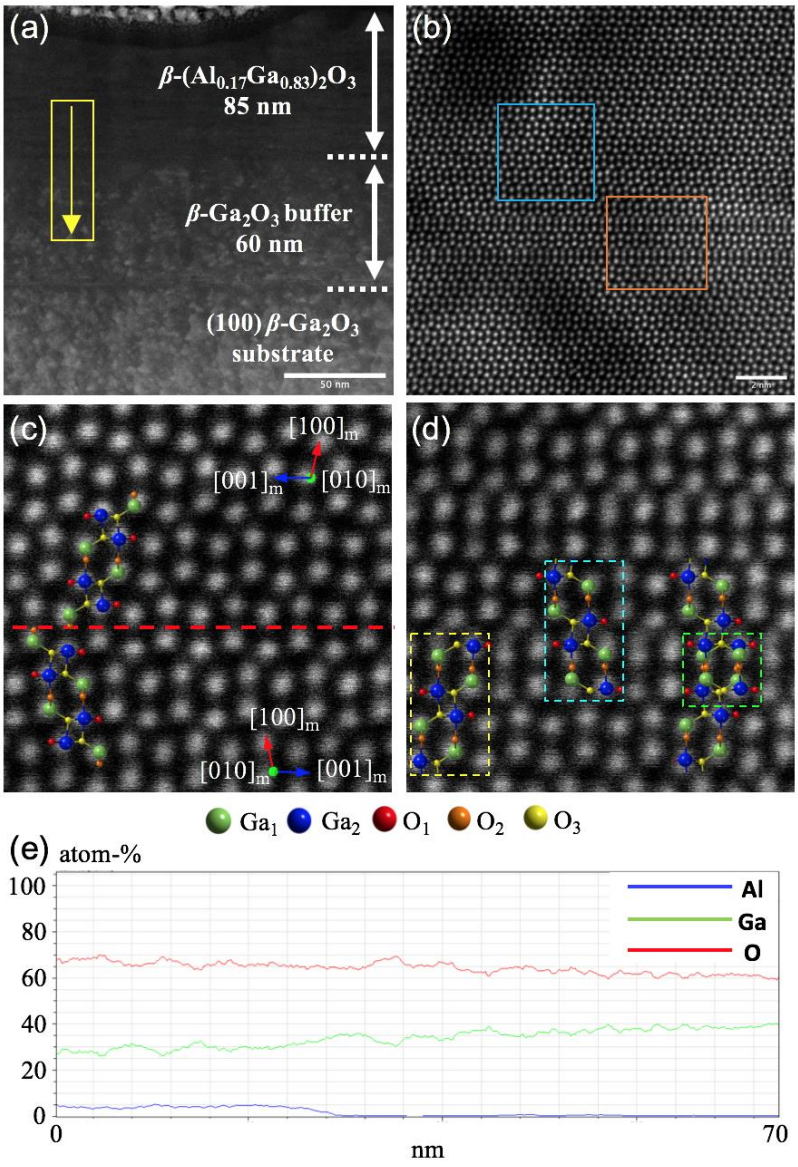
(a)
β-(Al0.17Ga0.83)2O3
85 nm
β-Ga2O3 buffer
60 nm
(100) β-Ga2O3
substrate
50 nm
(b)
(c)
[100]m
[001]m
[010]m
[100]m
[010]m
[001]m
(d)
Ga1 Ga2 O1 O2 O3
(e) atom-%
100
80
60
40
20
0
0
70
nm
Al
Ga
O

Figure 7

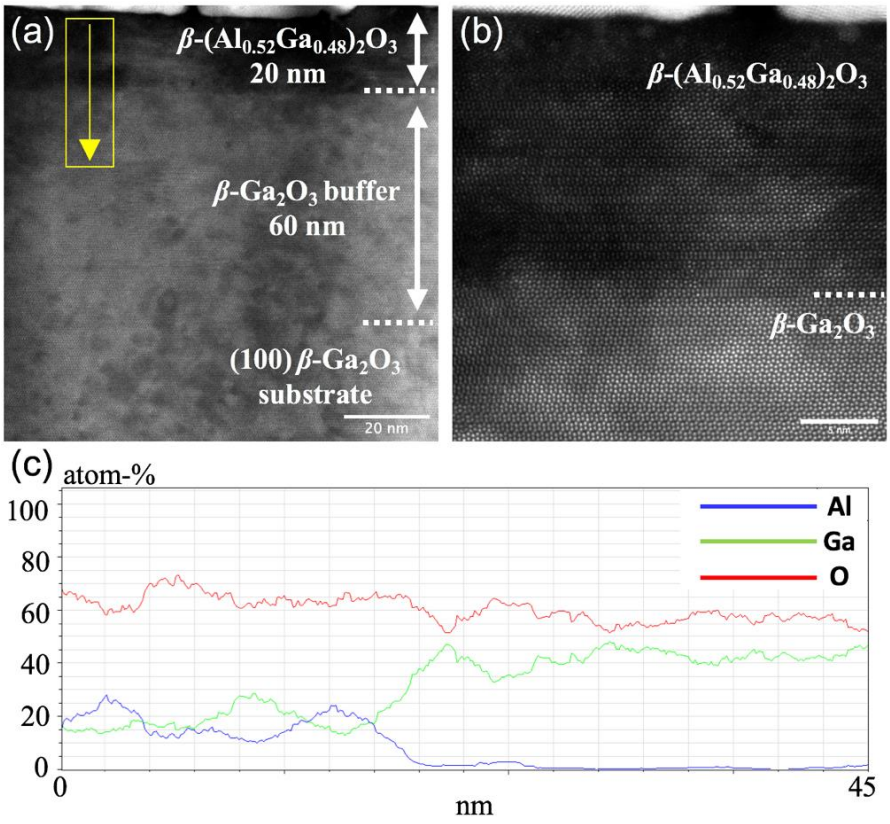
(a)
β-(Al0.52Ga0.48)2O3
20 nm
β-Ga2O3 buffer
60 nm
(100) β-Ga2O3
substrate
20 nm
(b)
β-(Al0.52Ga0.48)2O3
β-Ga2O3
(c)
atom-%
100
80
60
40
20
0
0
45
nm
Al
Ga
O

Figure 8

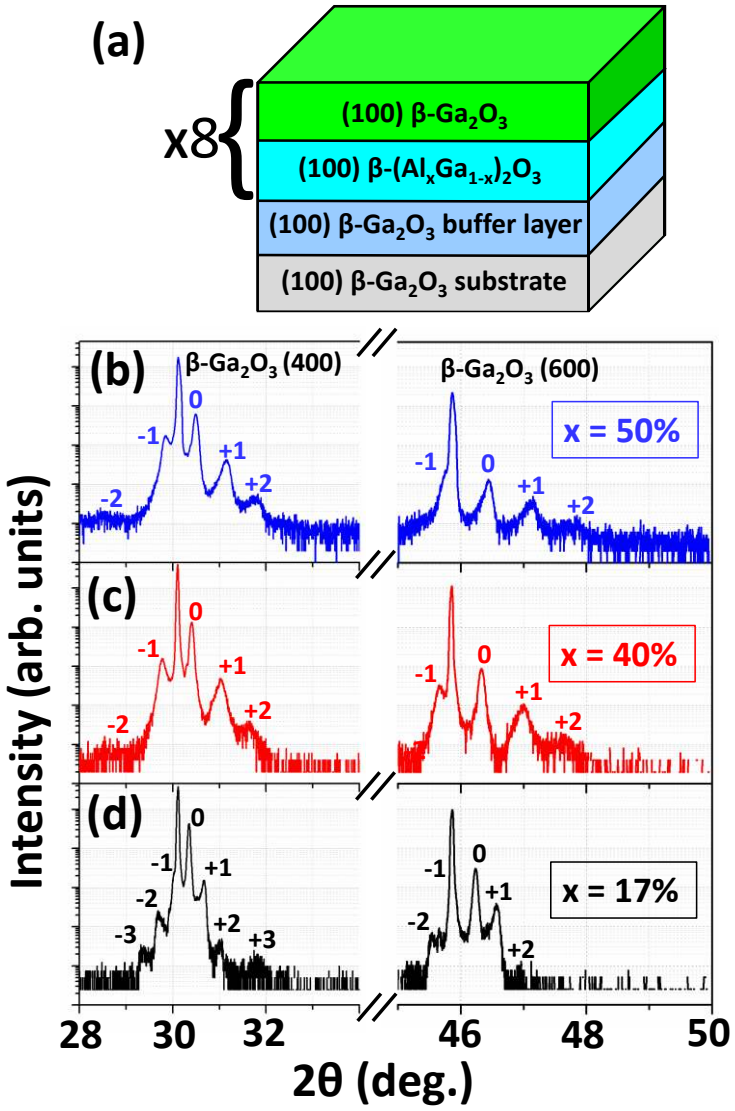
(a)
x8
(100) β-Ga2O3
(100) β-(AlxGa1-x)2O3
(100) β-Ga2O3 buffer layer
(100) β-Ga2O3 substrate
(b)
β-Ga2O3 (400)
β-Ga2O3 (600)
x = 50%
(c)
x = 40%
(d)
x = 17%
Intensity (arb. units)
2θ (deg.)
28
30
32
46
48
50

Figure 9

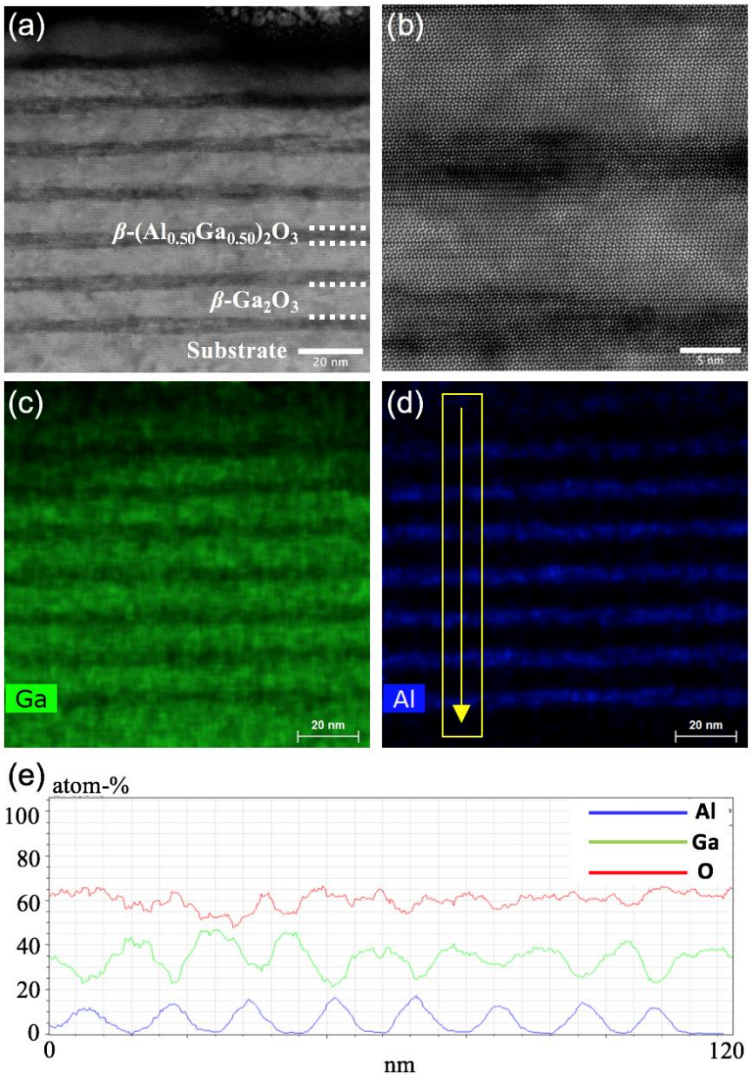
(a)
β-(Al0.50Ga0.50)2O3
β-Ga2O3
Substrate
20 nm
(b)
5 nm
(c)
Ga
20 nm
(d)
Al
20 nm
(e) atom-%
100
80
60
40
20
0
0
120
nm
Al
Ga
O